Molybdenum-Doped Manganese Oxide as a Highly Efficient and Economical Water Oxidation Catalyst

Balaghi, S Esmael ; Triana, Carlos A ; Patzke, Greta R

Abstract: The development of efficient and noble-metal-free electrocatalysts for the challenging oxygen evolution reaction (OER) is crucial for sustainable energy solutions. In this work, a facile coprecipitation method, followed by thermal postsynthetic treatment in N2/air, was developed to synthesize molybdenum-doped -Mn2O3 materials (Mn2O3:1.72%Mo, Mn2O3:2.64%Mo, Mn2O3:32.23%Mo, and Mn2O3:49.67%Mo) as low-cost water-oxidizing electrocatalysts. Powder X-ray diffraction (PXRD), extended X-ray absorption fine structure (EXAFS), X-ray photoelectron spectroscopy (XPS), and high-resolution transmission electron microscopy (HRTEM) investigations showed the presence of strong distortions in the molybdenum-doped -Mn2O3 host lattice (Mn2O3:2.64%Mo) and an average oxidation state of Mn2.8+. Several test assays demonstrated that these structural features significantly promote the OER activity. Mn2O3:2.64%Mo was found to exhibit very good activity among the series in cerium ammonium nitrate (CAN)-assisted water oxidation with a maximum turnover frequency (TOF) of 585 mol O2 m–2 h–1, which is a 15-fold improvement of the pure -Mn2O3 activity and higher than the value of the previously reported benchmark Mn-based catalyst, birnessite. The optimized catalyst (Mn2O3:2.64%Mo) excelled through a low onset potential (300 mV) and a promising overpotential of 570 mV for OER at a current density of 10 mA cm–2, which is only 20 mV above that of the noble metal benchmark RuO2 electrode and competitive with that of the most active Mn-based OER catalysts reported to date. Electrochemical impedance spectroscopy (EIS) studies demonstrated that the catalytically active surface area of Mn2O3:2.64%Mo is much higher than that of -Mn2O3 for the OER at the applied potential. In addition, stability during 30 h without degradation was achieved, which exceeds that of a wide range of current noble-metal-free electrocatalysts. Our study provides a facile and effective approach for the preparation of economical and high-performance manganese-based electrocatalysts for water oxidation.

DOI: https://doi.org/10.1021/acscatal.9b02718

Supporting Information

Molybdenum-Doped Manganese Oxide as a Highly Efficient and Economical Water Oxidation Catalyst

S. Esmael Balaghi, C. A. Triana, and Greta R. Patzke*

Department of Chemistry, University of Zurich, Winterthurerstrasse 190, CH-8057 Zurich, Switzerland

***Corresponding Author:** E-mail: greta.patzke@chem.uzh.ch

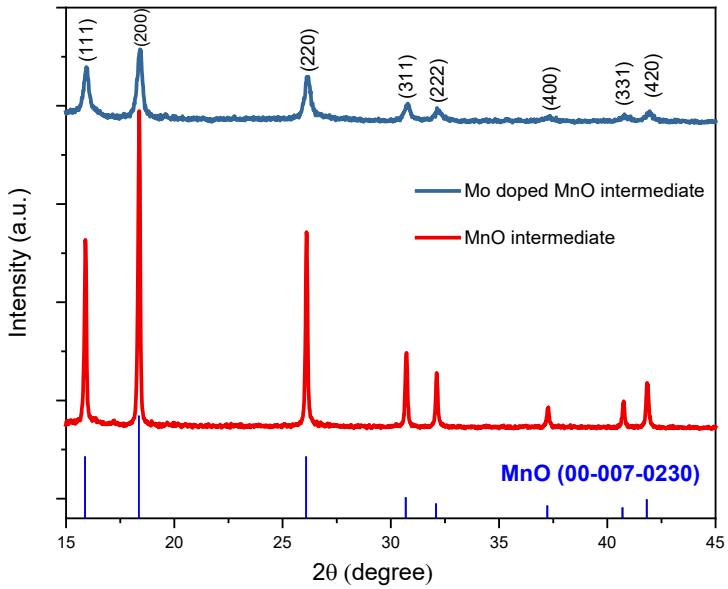

Figure S1. PXRD patterns of MnO and Mo doped MnO intermediates obtained after initial annealing in nitrogen.

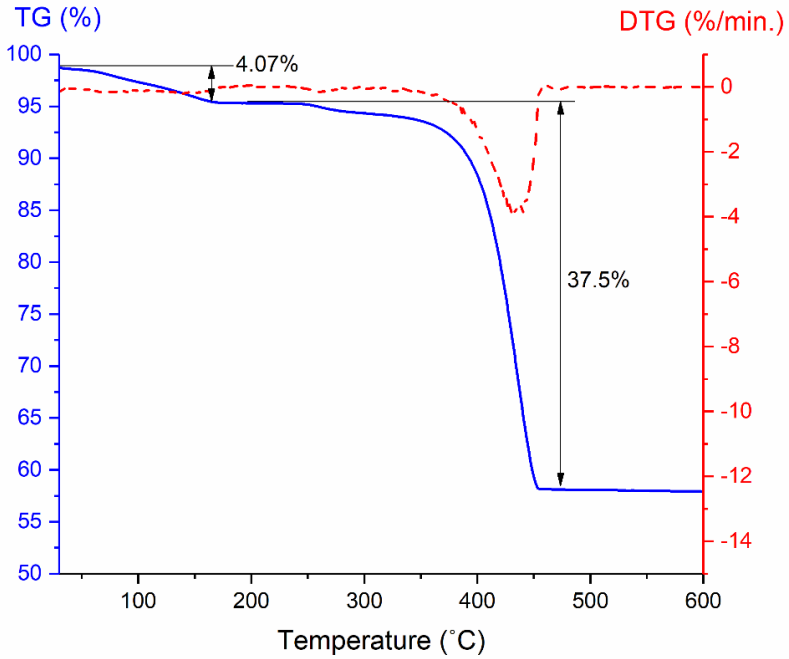

Figure S2. Thermogravimetric analysis (TGA) (blue solid line) and differential thermogravimetry analysis (DTG) (red dotted line) plots of the $MnCO_3$:2.64%Mo precursor thermally treated from room temperature to 600 ˚C in a nitrogen atmosphere at a heating rate of 5 ˚C min^{-1}.

Two distinct mass loss steps were observed during TGA. The first mass loss occurs below 150 ˚C, which is related to the release of physically or chemically absorbed water, while the second prominent mass loss between 140 ˚C and 600 ˚C corresponds to the thermal degradation of the carbonate precursor. The value obtained for the first mass loss is close to release of a water molecule (4.07% for $MnCO_3$:2.64%Mo) with DTG peaks at 150 ˚C. Similarly, the value observed for the second major mass loss can be attributed to the carbon dioxide (37.5% for $MnCO_3$:2.64%Mo) with distinct DTG signals at 435 ˚C.

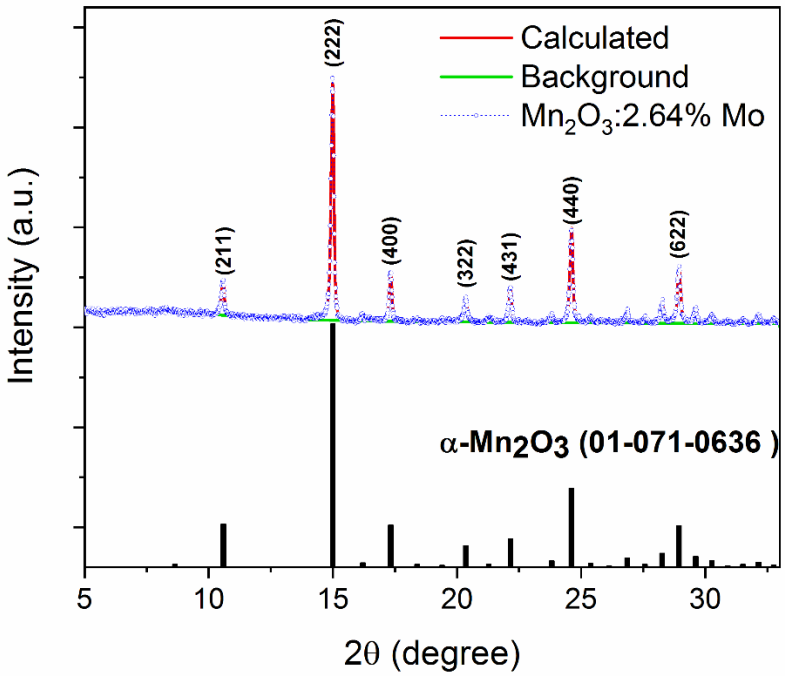

Figure S3. Rietveld refinement results of the PXRD pattern of Mn_2O_3:2.64%Mo after calcination at 400 °C in air.

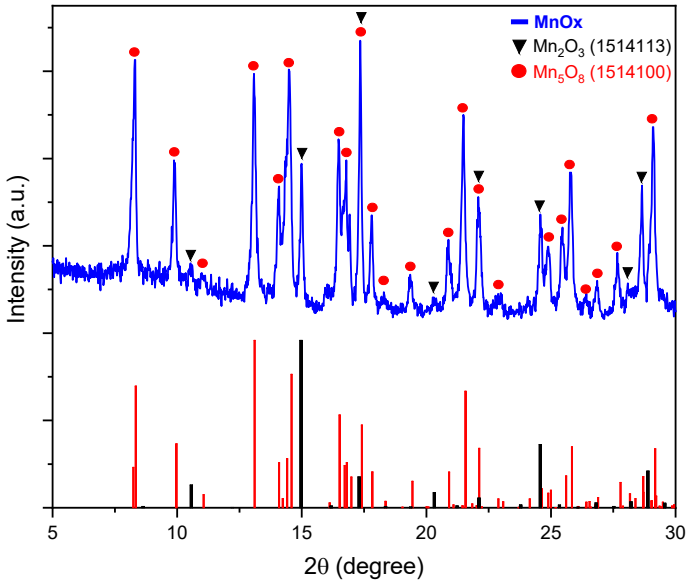

Figure S4. PXRD pattern of MnO_x obtained from annealing of pure manganese carbonate precursor at 400 °C in air.

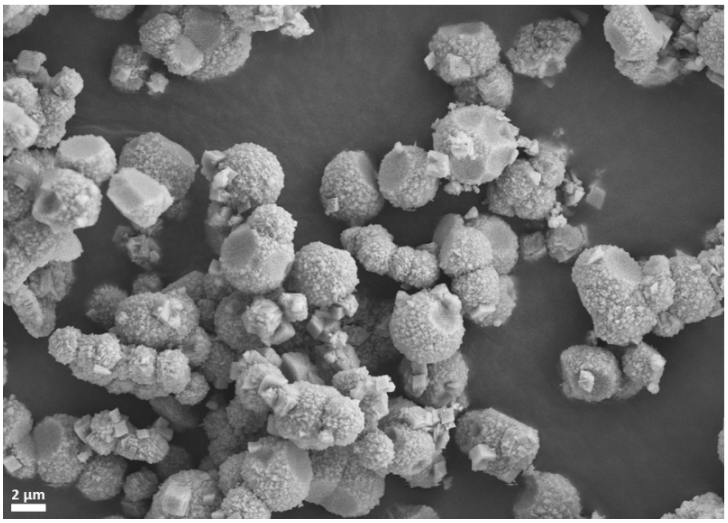

Figure S5. Representative SEM image of MnO_x.

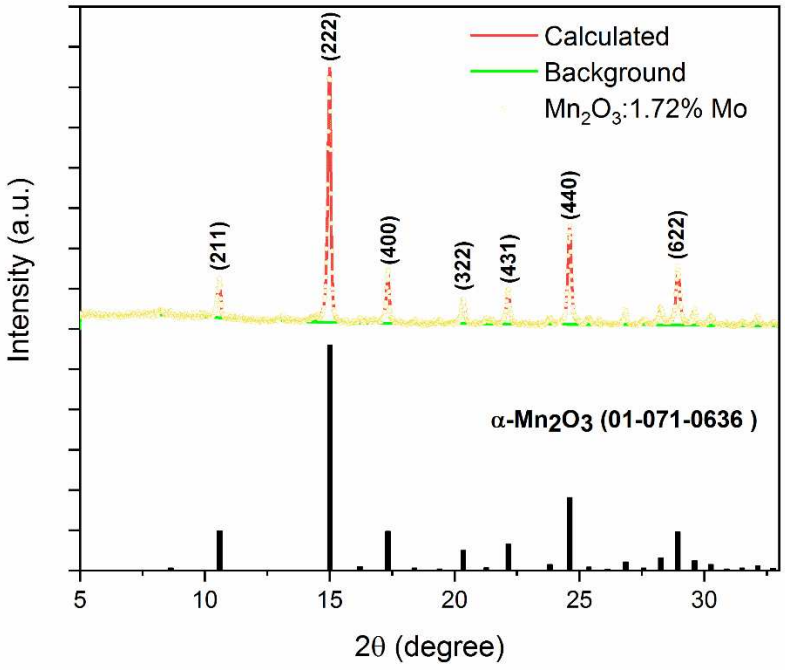

Figure S6. Rietveld refinement of the PXRD pattern of Mn_2O_3:1.72%Mo after calcination at 400 °C in air.

Table S1. Lattice parameters obtained from Rietveld refinement of the PXRD patterns of Mn_2O_3:2.64%Mo and Mn_2O_3:1.72%Mo after calcination to the final products.

Samples	Mn_2O_3:2.64%Mo	Mn_2O_3:1.72%Mo	**α-Mn_2O_3 (PDF 01-071-0636)**
Space group	*Ia-3* (206)	*Ia-3* (206)	*Ia-3* (206)
Lattice parameters (Å)			
a	9.4106(7)	9.4084(7)	9.41460(18)
b	9.4106(7)	9.4084(7)	9.41460(18)
c	9.4106(7)	9.4084(7)	9.41460(18)
R_{wp}	7.24	6.22	
Elements	Mn_2O_3:2.64%Mo x, y, z (**Occupancy**)	Mn_2O_3:1.72%Mo x, y, z (**Occupancy**)	
Mn1	0.000000 0.000000 0.000000 (**0.979**)	0.000000, 0.000000, 0.000000 (**0.990**)	
Mn2	0.28545(12), 0.000000, 0.250000 (**0.979**)	0.28483(10), 0.000000, 0.250000 (**0.990**)	
O	0.1287(4), 0.1466(4), -0.0826(4) (**1.000**)	0.1284(4), 0.1482(4), -0.0830(3) (**1.000**)	
Mo1	0.000000, 0.000000, 0.000000 (**0.021**)	0.000000, 0.000000, 0.000000 (**0.010**)	
Mo2	-0.021(17), 0.000000, 0.250000 (**0.021**)	0.586(12), 0.000000, 0.250000 (**0.010**)	

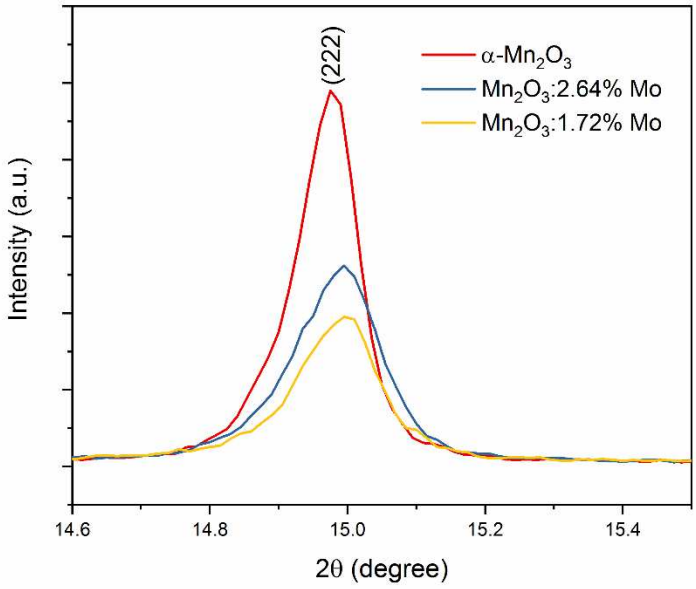

Figure S7. Relative shifts of the (222) PXRD peak for samples with different molybdenum contents.

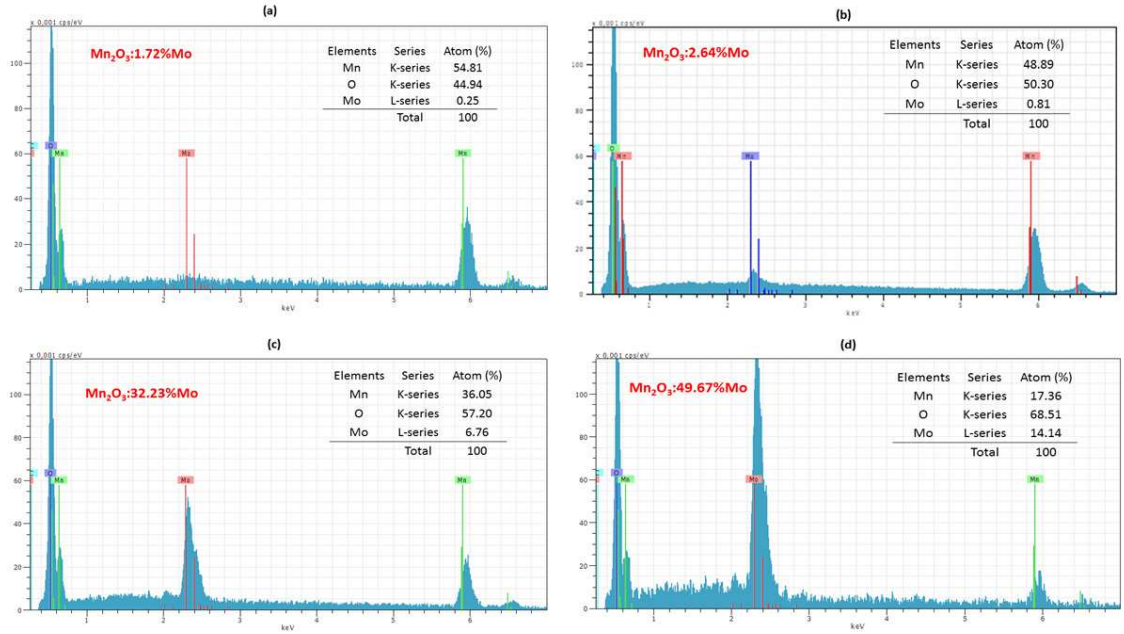

Figure S8. SEM-EDX of Mn_2O_3:1.72%Mo, Mn_2O_3:2.64%Mo, Mn_2O_3:32.23%Mo and Mn_2O_3:49.67%Mo.

Table S2. Determination of manganese and molybdenum ratios in Mn_2O_3:1.72%Mo, Mn_2O_3:2.64%Mo, Mn_2O_3:32.23%Mo and Mn_2O_3:49.67%Mo obtained from EDX and ICP-MS analyses.

Sample	**Initial Mo:Mn atomic percentage ratio**	**Mo:Mn atomic percentage ratio (SEM-EDX)**	**Mo:Mn atomic percentage ratio (ICP-MS)**
Mn_2O_3:1.72%Mo	1 : 4	1 : 219.00	1 : 81
Mn_2O_3:2.64%Mo	1 : 2	1 : 60.00	1 : 46
Mn_2O_3:32.23%Mo	1 : 1	1 : 5.30	1 : 2
Mn_2O_3:49.67%Mo	1 : 0.66	1 : 1.20	1.08 : 1

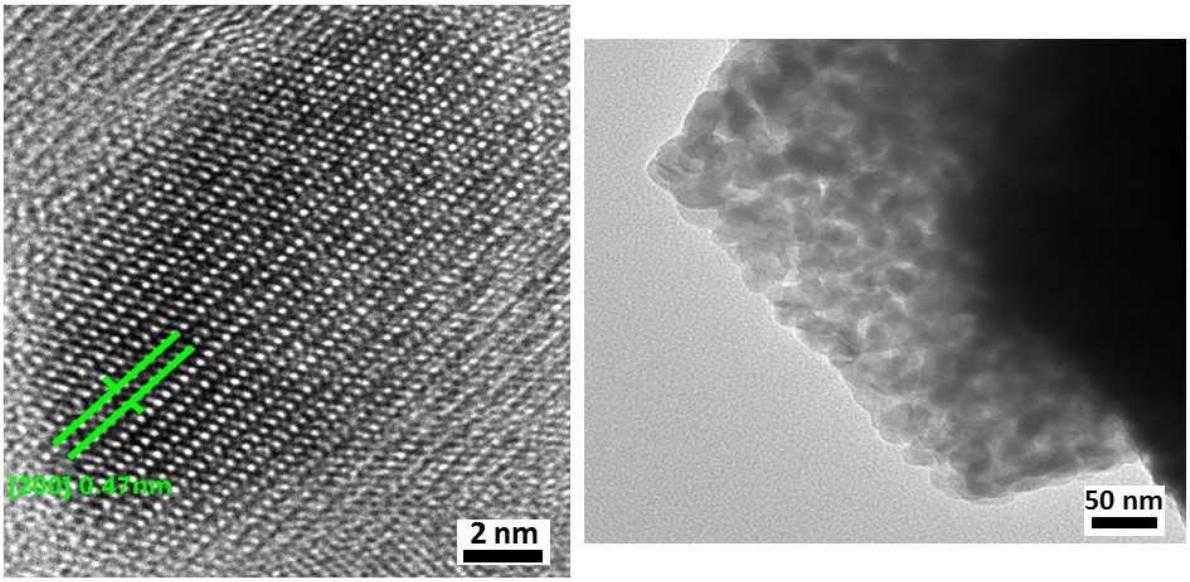

Figure S9. Representative HRTEM images of Mn_2O_3:2.64%Mo.

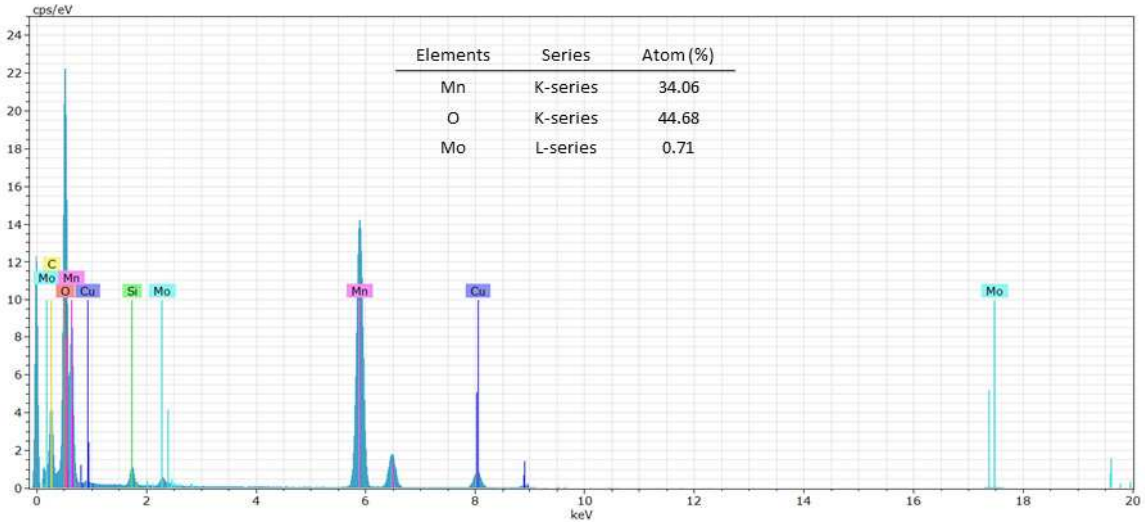

Figure S10. Quantitative STEM-EDX analysis of Mn_2O_3:2.64%Mo.

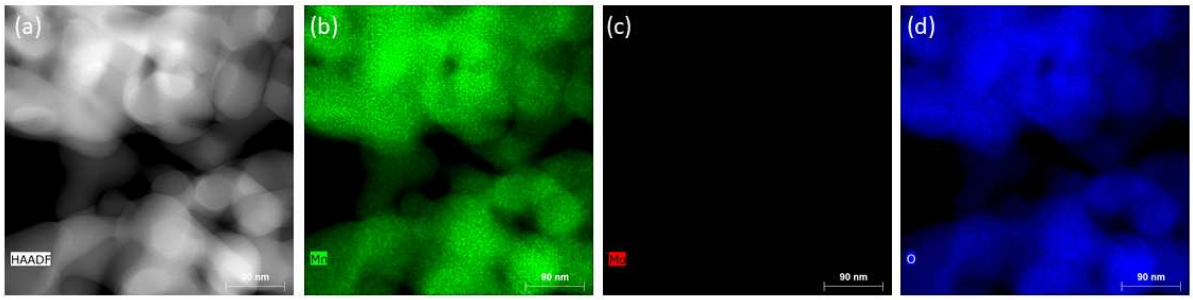

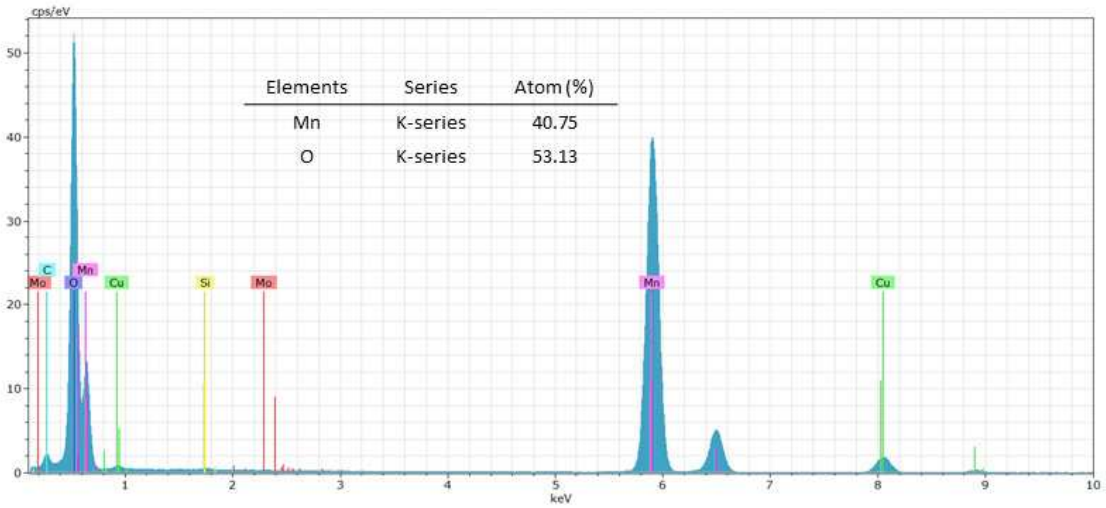

Figure S11. HAADF-STEM-EDX mapping (top) and quantitative EDX analysis of α-Mn_2O_3 (bottom).

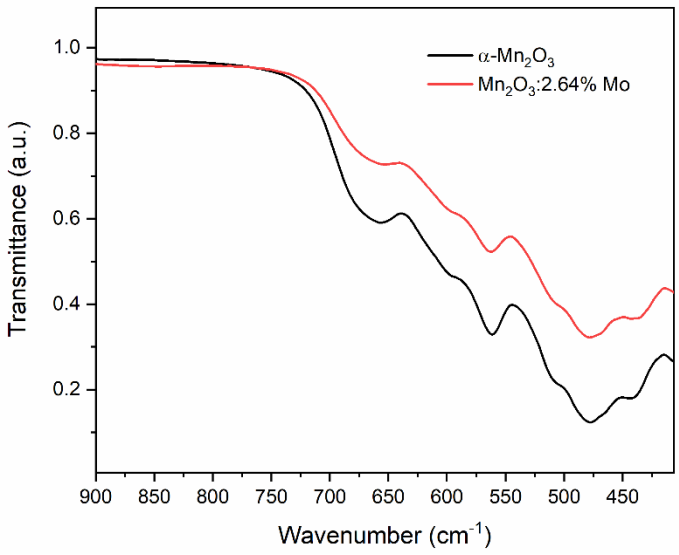

Figure S12. FT-IR spectra of α-Mn_2O_3 and Mn_2O_3:2.64%Mo.

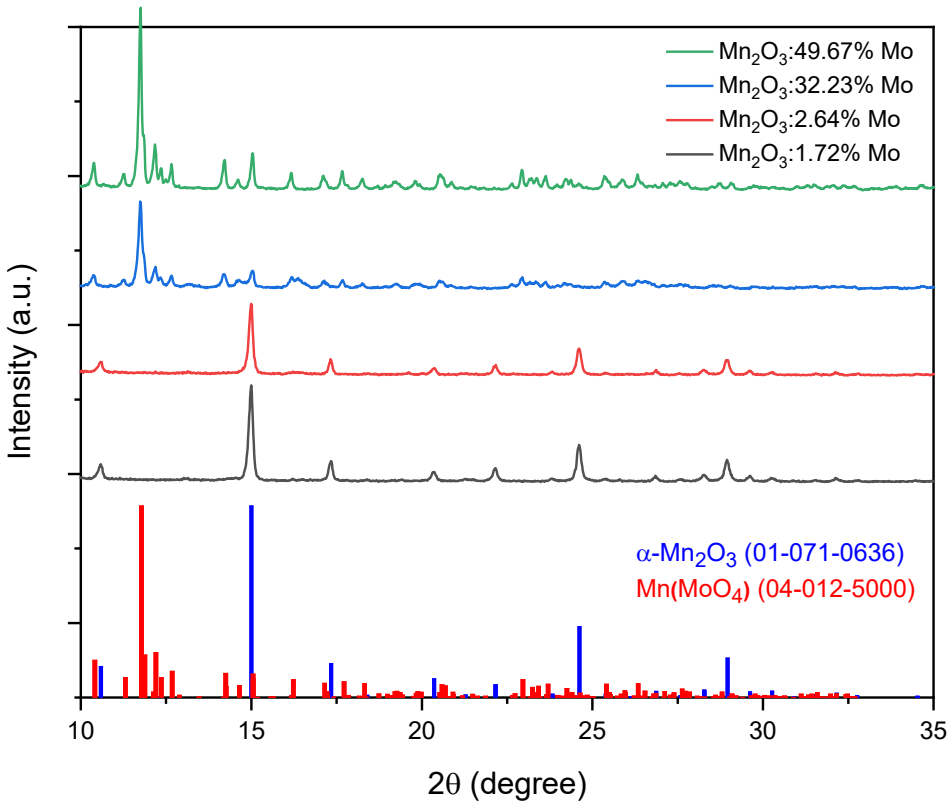

Figure S13. PXRD patterns of Mn_2O_3:1.72%Mo, Mn_2O_3:2.64%Mo, Mn_2O_3:32.23%Mo and Mn_2O_3:49.67%Mo samples with different molybdenum contents.

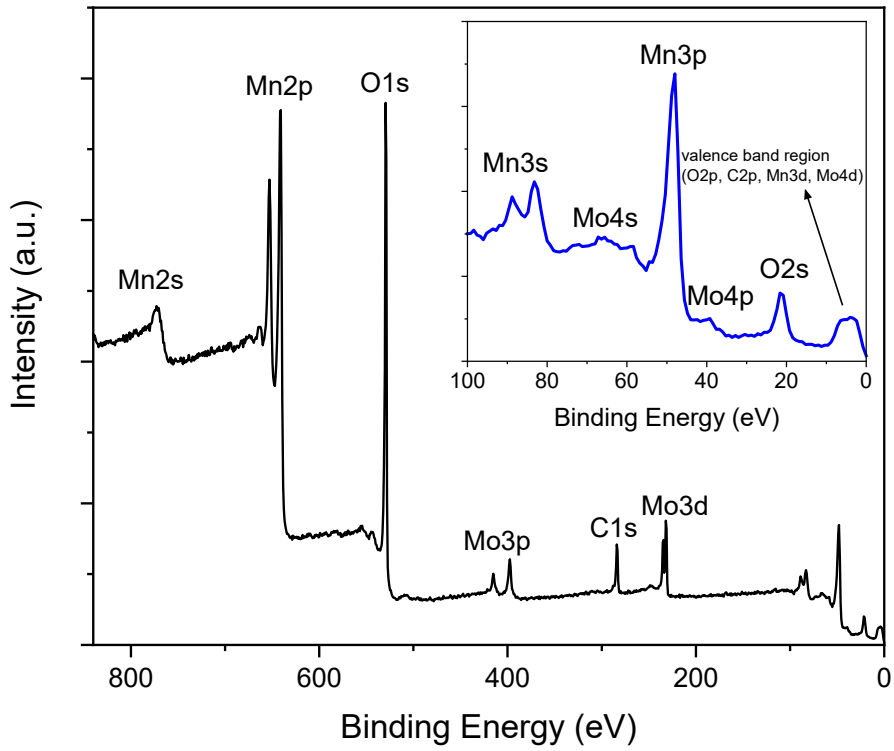

Figure S14. Survey XPS spectrum of Mn_2O_3:2.64%Mo.

Reaction 1:

$$Mo^{6+}Mn_{46}{}^{2+}CO_3 \text{ containing } NH^{4+} \text{ residues} \xrightarrow[400°C\ (12°C\ min^{-1})]{N_2\ (60\ ml\ min^{-1})} Mo^{<6+}Mn_{46}{}^{2+}O_x$$

Reaction 2:

$$Mo^{<6+}Mn_{46}{}^{2+}O_x \xrightarrow[400°C\ (12°C\ min^{-1})]{Air} Mo^{<5+}Mn_{46}{}^{<3+}O_x$$

Reaction 3:

$$(NH_4)_6(Mo_7{}^{6+}O_{24})(H_2O)_4 \xrightarrow[400°C\ (12°C\ min^{-1})]{N_2\ (60\ ml\ min^{-1})} MoO_3 + Mo_4O_{11}$$

Figure S15. Schematic representation of the changes in the valence state of Mo and Mn species under different annealing reaction conditions.

Table S3. CHN elemental analysis of the $MnCO_3$:2.64%Mo precursor and Mn_2O_3:2.64%Mo.

Samples	Carbon (wt%)	Hydrogen (wt%)	Nitrogen (wt%)
$MnCO_3$:2.64%Mo precursor	5.12	1.11	1.25
Mn_2O_3:2.64%Mo	0.17	0.02	0.00

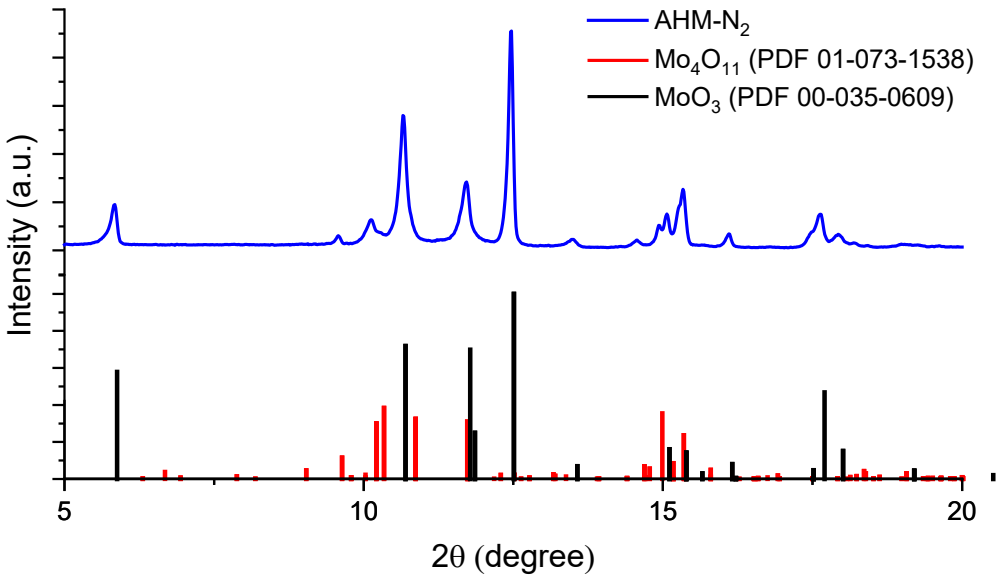

Figure S16. PXRD patterns of AHM-N_2 and related PXRD references.

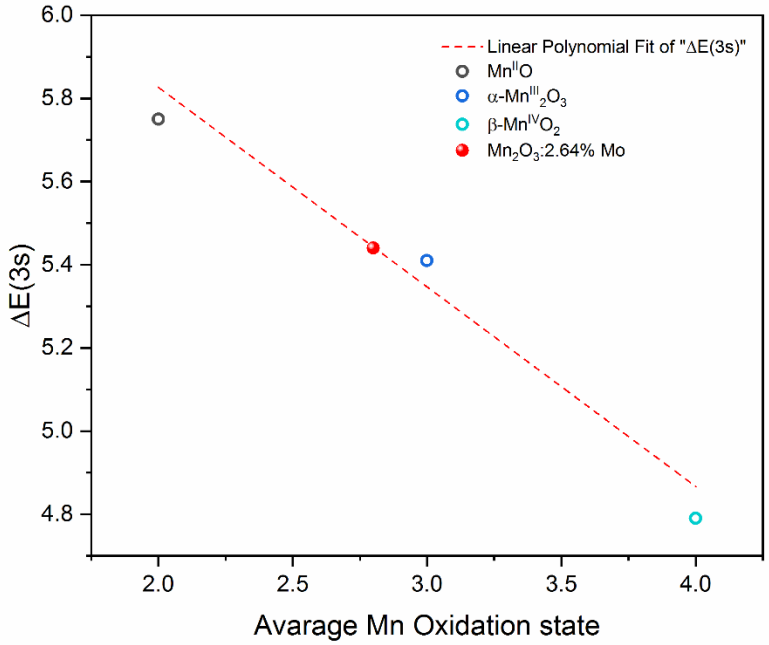

Figure S17. XPS linear calibration for quantification of the main Mn oxidation state of Mn_2O_3:2.64%Mo (red dots) based on the ΔE(3s) binding energy of reference compounds $Mn^{II}O$, α-$Mn^{III}_2O_3$, and β-$Mn^{IV}O_2$.

Table S4. Calculated main values for the coordination numbers (*N*), amplitude reduction factors (S_0^2), interatomic distances (R) and Debye-Waller factors (σ^2) obtained from nonlinear least-squares fitting of the experimental Mn *K*-edge EXAFS spectra FT|$k^3\chi(k)$| of α-Mn_2O_3 and Mn_2O_3:2.64%Mo.

Sample	Bonds	N	S_0^2	σ^2	ΔE_0	R(Å)
α-Mn_2O_3	Mn-O	2.0	1.05	0.00038	0.295	1.91286
	Mn-O	2.0	1.05	0.00255	0.295	2.07682
	Mn-O	2.0	1.05	0.00868	0.295	2.26757
	Mn-Mn	4.0	1.05	0.00297	0.295	3.09843
	Mn-Mn	2.0	1.05	0.00056	0.295	3.18621
	Mn-Mn	2.0	1.05	0.00988	0.295	3.60481
Mn_2O_3:2.64%Mo	Mn-O	2.0	1.05	0.00268	0.352	2.04002
	Mn-O	1.8	1.05	0.00328	0.352	1.89552
	Mn-O	2.0	1.05	0.01197	0.352	2.25936
	Mn-Mn	4.0	1.05	0.00347	0.352	3.10902
	Mn-Mo	2.0	1.05	0.00302	0.352	3.10043
	Mn-Mn	4.0	1.05	0.01485	0.352	3.61941

The α-Mn_2O_3.cif structure file was obtained from the ICDD database (PDF 01-071-0636).

Table S5. BET surface area and TOF of catalysts (10 mg) for the chemical water oxidation reaction in the presence of 0.11 M CAN solution.

Catalysts	S_{BET} (m^2 g^{-1})	TOF (mmol O_2 m^{-2} h^{-1})	TOF (µmol O_2 m^{-2} h^{-1})	TOF (mmol O_2 h^{-1} g Cat.$^{-1}$)	TOF (mmol O_2 h^{-1} mmol Mn^{-1})
Mn_2O_3:1.72%Mo	27	0.4	353	9.9	0.7
Mn_2O_3:2.64%Mo	**33**	**0.6**	**585**	**19.1**	**1.5**
Mn_2O_3:32.23%Mo	28	0.01	11	0.3	0.04
Mn_2O_3:49.67%Mo	29	0.0	0.0	0.0	0.0
MoO_2 and α-Mn_2O_3 physical mixture	26	0.03	28	0.7	-
α-Mn_2O_3	16	0.04	37	0.6	0.05

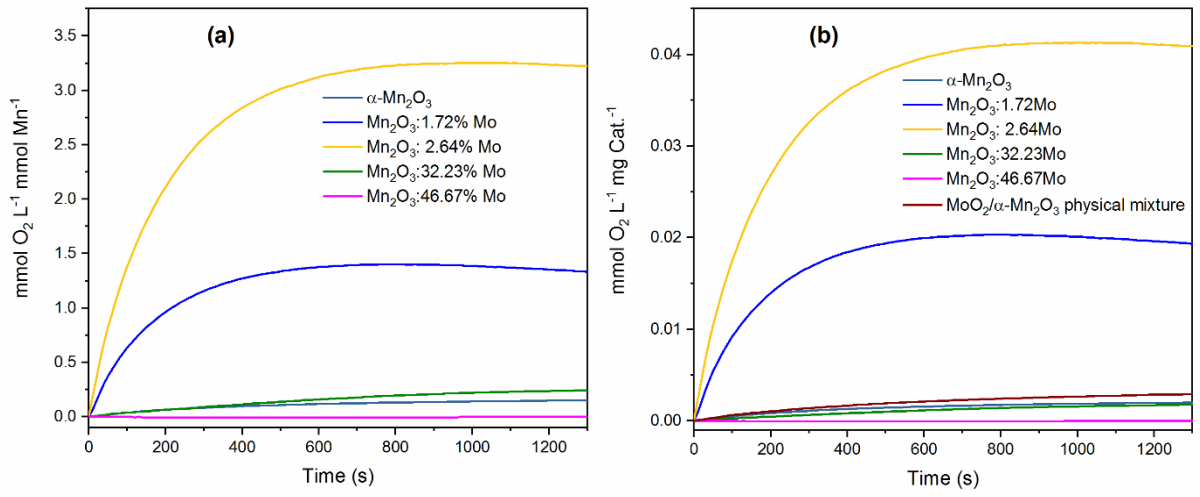

Figure S18. Dissolved oxygen concentrations of catalysts (10 mg) measured with a LDO electrode in deoxygenated aqueous solutions containing 0.11 M CAN as oxidant. The activity is normalized based on mmol of Mn content (a) and mg of catalyst (b).

Table S6. Comparison of the chemical water oxidation activities in the presence of CAN solution among different reported Mn-based oxides.

Catalyst	S_{BET} (m^2 g^{-1})	CAN concentration (M)	TOF (µmol O_2 m^{-2} h^{-1})	TOF (mmol O_2 h^{-1} mmol Mn^{-1})	Reference
Mn_2O_3:2.64%Mo	32.7	0.11	583.20	1.5	This work
	32.7	0.25	649.54	1.46	This work
α-Mn_2O_3 (bixbyite)	16.6	0.11	36.70	0.05	This work
	16.6	0.25	56.92	0.07	This work
	22	0.25	50.00	0.090	[1]
Mn_3O_4 (Hausmannite)	11	0.25	0.00	0.000	[1]
$LiMn_2O_4$	70	0.25	10.00	0.050	[1]
$Ca_{0.48}MnO_{1.93}$ (Marokite)	1	0.25	285.00	0.030	[1]
MnO (Manganosite)	2	0.25	0.00	0.000	[1]
$MnO_{1.95}·0.1H_2O$ (Pyrolusite)	12	0.25	15.00	0.010	[1]
$MnO_{1.85}·0.3H_2O$ (Ramsdellite)	95	0.25	50.00	0.425	[1]
$K_{0.07}MnO_{1.94}$ (Cryptomelane)	125	0.25	25.00	0.300	[1]
$MnO_{1.95}·0.4H_2O$ (Hollandite)	80	0.25	40.00	0.275	[1]
$K_{0.11}Ca_{0.22}MnO_{2.03}·0.7H_2O$ (Todorokite)	250	0.25	50.00	1.375	[1]
$Ca_{0.21}MnO_{2.16}·1.3H_2O$ (Birnessite)	240	0.25	60.00	1.650	[1]
$Na_{0.15}K_{0.51}MnO_{2.25}·0.9H_2O$ (Vernadite)	160	0.25	20.00	0.425	[1]

Table S7. Comparison of the photochemical water oxidation activities in the presence of $Na_2S_2O_8$ as two-electron acceptor and $Ru(bpy)_3^{2+}$ as photosensitizer among different reported Mn-based oxides.

Catalyst	S_{BET} (m^2 g^{-1})	pH	O_2 detection method	TOF (µmol O_2 m^{-2} s^{-1})	Reference
Mn_2O_3:2.64%Mo	32.7	8.5 (borate buffer)	Clark electrode	1.5	This work
α-Mn_2O_3 (bixbyite)	16.6	8.5 (borate buffer)	Clark electrode	0.77	This work
	16.27	7 ($NaHCO_3$)	Clark electrode	0.29	[2]
Mn_3O_4 (hausmannite)	27.22	7 ($NaHCO_3$)	Clark electrode	0.068	[2]
λ-MnO_2 (spinel)	121.1	7 ($NaHCO_3$)	Clark electrode	0.0078	[2]
$LiMn_2O_4$ (spinel)	24.5	7 ($NaHCO_3$)	Clark electrode	<LOD [a]	[2]
α-MnO_2 (cryptomelane-type)	74.58	7 ($NaHCO_3$)	Clark electrode	<LOD	[2]
δ-MnO_2 (birnessite)	17.88	7 ($NaHCO_3$)	Clark electrode	<LOD	[2]
β-MnO_2 (pyrosulite)	14.92	7 ($NaHCO_3$)	Clark electrode	<LOD	[2]
R-MnO_2 (ramsdellite)	89.27	7 ($NaHCO_3$)	Clark electrode	<LOD	[2]

[a] Limit of detection

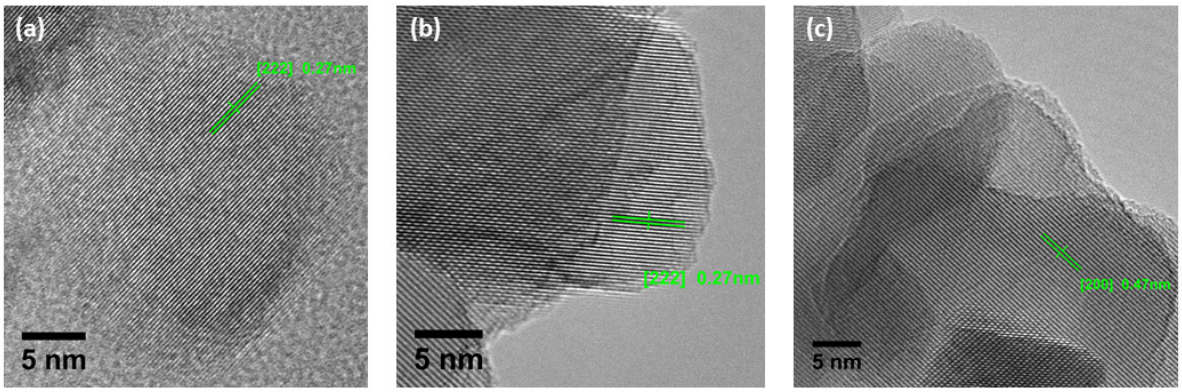

Figure S19. Post-catalytic HRTEM images of Mn_2O_3:2.64%Mo after (a) chemical and (b, c) photochemical water oxidation.

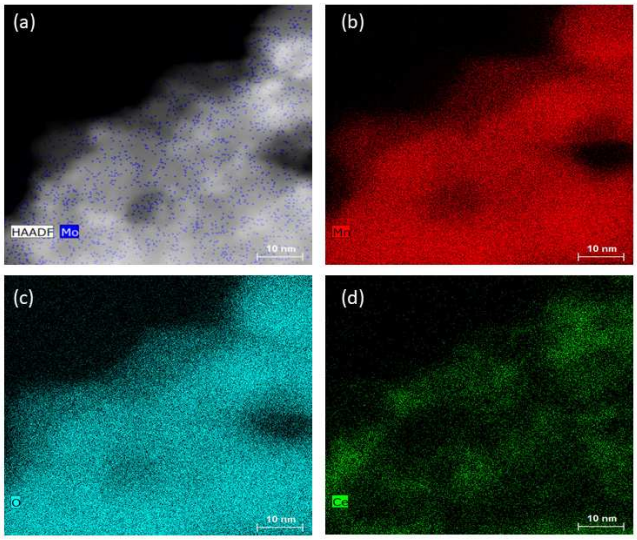

Figure S20. HAADF STEM-EDX mapping of Mn_2O_3:2.64%Mo after chemical water oxidation in the presence of 0.11 M CAN solution.

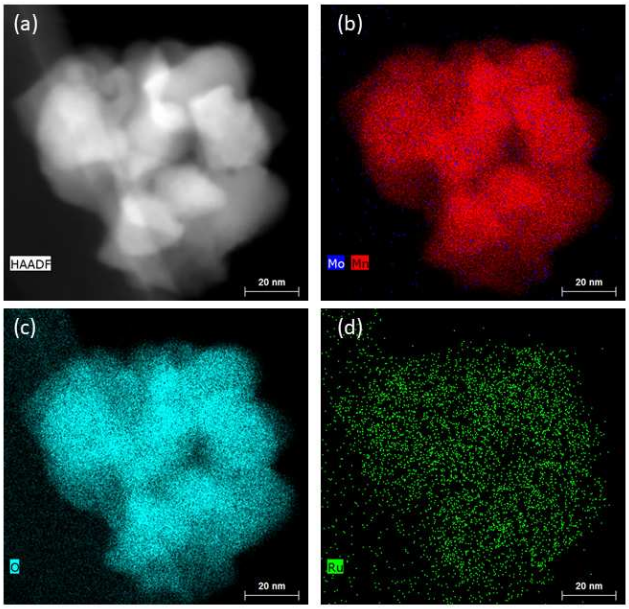

Figure S21. HAADF STEM-EDX mapping of Mn_2O_3:2.64%Mo after photochemical water oxidation in the presence of 1mM $Ru(bpy)_3^{2+}$ solution.

Table S8. Comparison of the electrochemical OER activities among different reported Mn-based catalysts.

Catalyst	Electrolyte	Current density j ($mA\ cm^{-2}$)	Overpotential η vs RHE (mV)	Tafel slope ($mV\ per\ dec^{-1}$)	Reference
Mn_2O_3:2.64%Mo	1 M KOH	**10**	**570**	**75**	This work
α-Mn_2O_3	1 M KOH	10	730	109	This work
Mn_2O_3	0.1M KOH	10	580	n.a.	[3]
α-MnO_2 treated by ionic liquid	1 M KOH	10	394	49	[4]
MnO_x/N-CNT	1 M KOH	10	360	75	[5]
Cs^+ intercalated MnO_2 nano-sheet	1 M KOH	5	613	101.3	[6]
MnO_2 nano-sheet on Ni foam	1 M KOH	10	320	40	[7]
α-MnO_2	1 M KOH	10	450	73.1	[8]
α-MnO_2/β-MnO_2	1 M KOH	10	510	100.0	[8]
β-MnO_2	1 M KOH	10	600	109.3	[8]
Broken β-MnO_2	1 M KOH	10	580	101.5	[8]
MnO_x nanowire	1 M KOH	10	590	106	[9]
δ-MnO_2 **extracted from theoretical calculations*	pH = 0	1	590	n.a.	[10]
Li-Birnessite	1 M KOH	1	740	n.a.	[11]
Co doped α-MnO_2	0.1 M KOH	1	770	57	[12]
Ru doped α-MnO_2	0.1 M KOH	1	680	62	[12]
$CaMn_xO_y$	0.66 mM phosphate buffer, pH = 7	1.5	550	n.a.	[13]
MnO	0.1 M KOH	10	610	n.a.	[3]
TiO_2/MnO_x nanowire	1 M KOH	1	524	n.a.	[14]
tetragonal cryptomelane type MnO_2	0.1 M KOH	10	490	77.5	[15]
β-MnO_2	1 M KOH	10	500	n.a.	[16]
α-Mn_2O_3 film	1 M KOH	20	570	n.a.	[17]
Partially oxidized MnO	300 mM phosphate buffer, pH = 7.8	5	530	n.a.	[18]

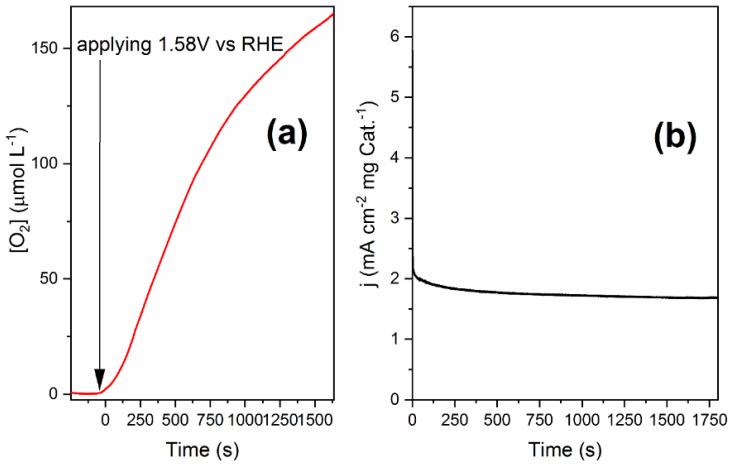

Figure S22. Simulated alkaline seawater electrolysis with the Mn_2O_3:2.64%Mo catalyst in 1.0 M KOH + 0.5 M NaCl. Oxygen evolution (a) by Mn_2O_3:2.64%Mo at 1.58 mV (vs. RHE) with only 50 mV above onset potential in amperometry (b).

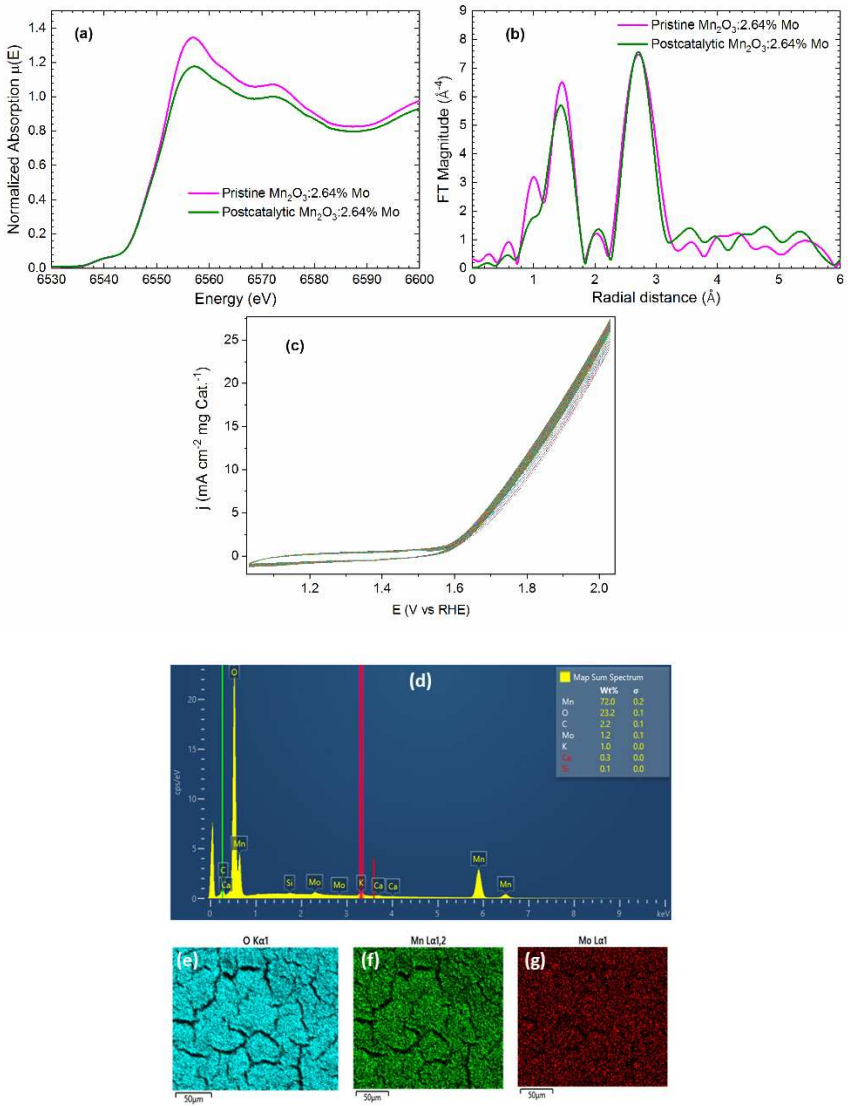

Figure S23. (a) Mn *K*-edge XANES and (b) FT|$k^3\chi$(k)| spectra of pristine and postcatalytic Mn_2O_3:2.64%Mo. 100 CV cycles of FTO/ Mn_2O_3:2.64%Mo electrode in 1.0 M KOH solution in the potential range between 0.0 and 1.0 V at a scan rate of 5 mV/s. (d-g) SEM-EDX analysis of Mn_2O_3:2.64%Mo after 100 CV cycles.

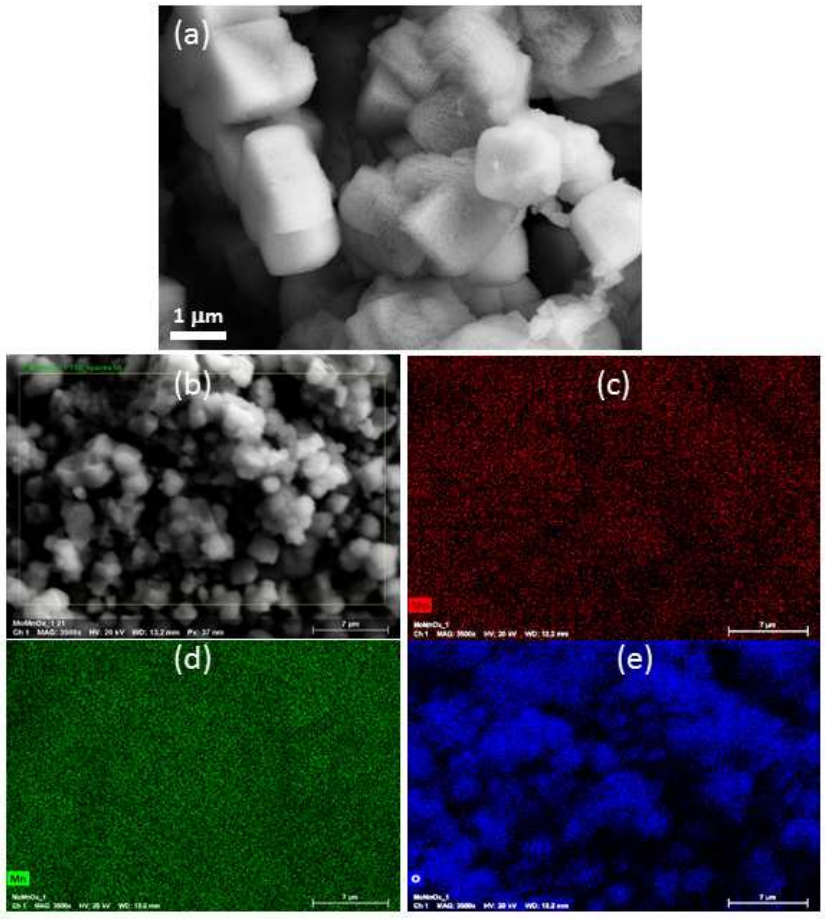

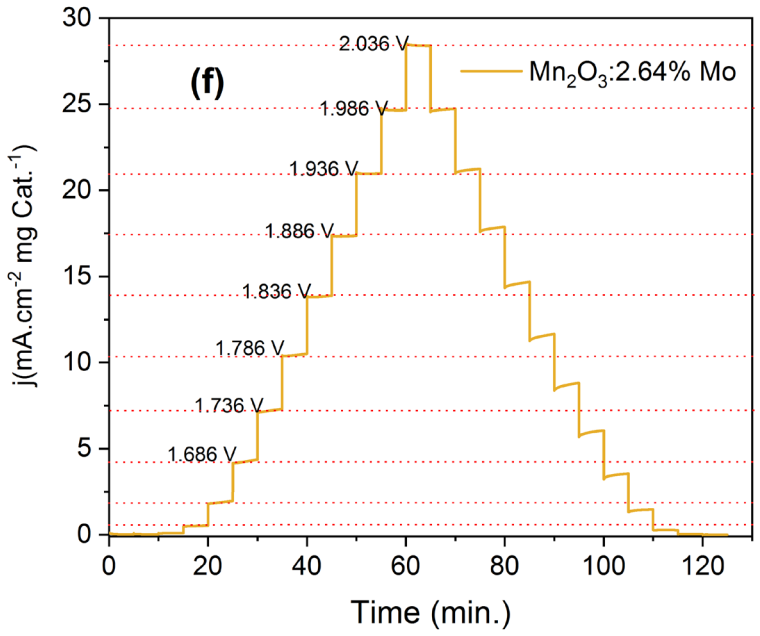

Figure S24. SEM-EDX mapping (a-e) of Mn_2O_3:2.64%Mo after multi-potential-step chronoamperometry (f) in 1.0 M KOH solution with a potential step of 0.05 V amperometry in the potential range of 1.43 to 2.03 V.

Table S9. Comparison of the electrochemical OER activities among different reported noble metal-free catalysts.

Catalyst	Electrolyte	Current density j (mA cm^{-2})	Overpotential η vs RHE (mV)	Tafel slope (mV per dec^{-1})	Reference
Mn_2O_3:2.64%Mo	1 M KOH	10	570	75	This work
Co_3O_4/N graphene	0.1 M KOH	10	960	121.8	[19]
$CoFe_2O_4$@CoFe-Bi	0.1 M $K_2B_4O_8$	10	460	127	[20]
NiFe/Ni Co_2O_4	1 M KOH	10	340	38.8	[21]
NiFeOH/NiFeP	1 M KOH	10	258	39	[22]
$NiPS_3$@NiOOH	0.1 M KOH	10	350	80	[23]
$Ni_{0.75}$-$V_{0.25}$ LDH narrow nanosheets	1 M KOH	10	350	50	[24]
Ni-FeOH@Ni_3S_2	1 M KOH	10	479	124	[25]

The impedance of the CPE can be calculated by $Z_{CPE} = \frac{1}{\text{CPE}\,(j\omega)^n}$ where ω is the angular frequency (ω = 2πf, f is frequency), j is the imaginary number, $\sqrt{-1}$. The range of n can be varied between $1 \geq n \geq 0$, where for n=0 the CPE acts as a resistor and for n=1, the CPE acts as an ideal capacitor.[26] The real capacitance of the double layer, C_{dl}, can be calculated from CPE_{dl} using $C_{dl} = R^{(\frac{1-n}{n})} CPE_{dl}{}^{(\frac{1}{n})}$.[27,28] The C_{dl} was calculated as 0.167 μF cm^{-2} and 311 μF cm^{-2} for α-Mn_2O_3 and Mn_2O_3:2.64%Mo, respectively. The value of the C_{dl} is directly proportional to the active surface area of the electrode.[29]

Table S10. Equivalent circuit and its parameters for FTO/catalyst in 1.0 M KOH solution obtained from the Nyquist plots of Figure 19a.

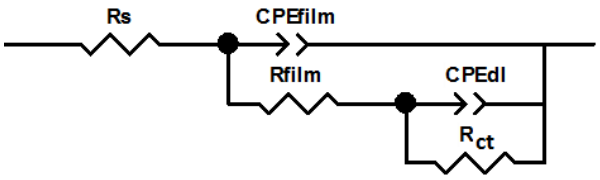

	Value	
Element	**α-Mn_2O_3**	**Mn_2O_3:2.64%Mo**
R_S	38.45	11.50
CPE_{film}-T	8.92×10^{-7}	5.5×10^{-7}
CPE_{film}-P	0.70	0.85
R_{film}	7310	818.80
CPE_{dl}-T	6.73×10^{-7}	3.61×10^{-4}
CPE_{dl}-P	0.72	0.53
R_{ct}	38303	2339

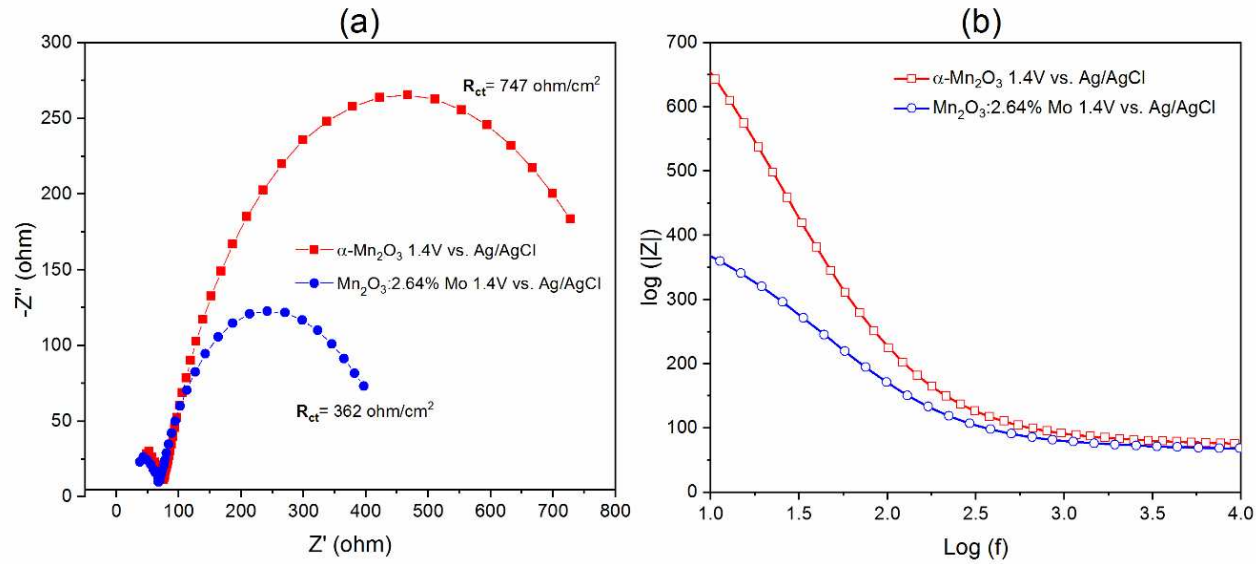

Figure S25. (a) Nyquist diagram and (b) Bode plots of FTO/ Mn_2O_3:2.64%Mo (blue line), and FTO/ α-Mn_2O_3 (red line) in a 0.1 M KPi buffer solution at 1.4 V applied potential in the frequency range of 0.1 Hz-50 kHz.

Calibration of the Ag|AgCl reference electrode

Concerning the calibration of the Ag|AgCl reference electrode vs. RHE, we proceeded as follows: The Ag|AgCl|KCl 3M reference electrode was calibrated with respect to the reversible hydrogen electrode (RHE), in 1.0 M H_2SO_4 (pH ≈ 0) electrolyte using Pt as working and counter electrodes, while purging with high purity hydrogen gas during the measurement.[30,31] The calibration value was 0.210 V, which is almost 0.05 V higher than the reported value for the Ag|AgCl|KCl 3 M reference electrode. To calculate the $E_{1/2}$ value, we took the average value of potential where the anodic and cathodic scans crosses the zero current axis. The measured potentials vs. Ag/AgCl were converted to the reversible hydrogen electrode (RHE) scale according to the Nernst equation: $E_{RHE} = E_{Ag/AgCl} + 0.059\ pH + 0.210$, where E_{RHE} is the converted potential vs. RHE and $E_{Ag/AgCl}$ is the experimentally measured potential against the Ag/AgCl reference.

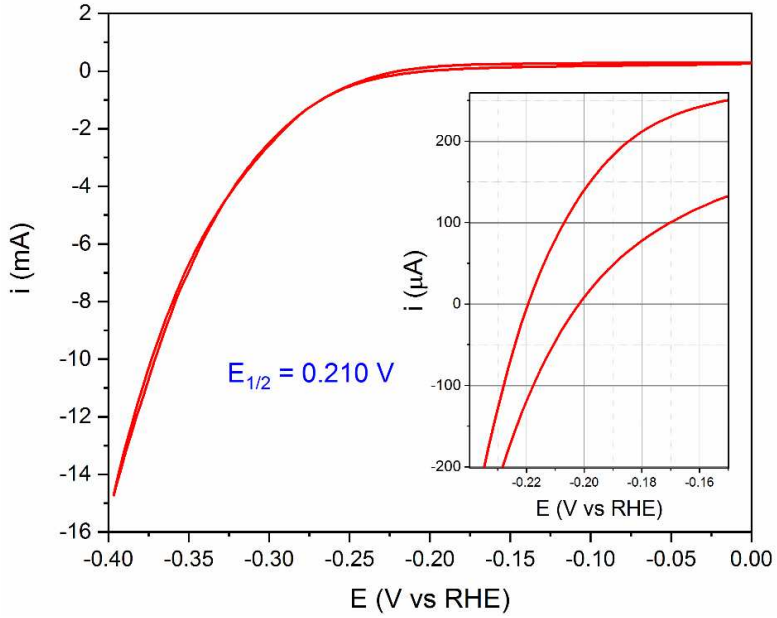

Figure S26. Calibration of reference electrode (Ag|AgCl|KCl 3 M) with respect to Reversible Hydrogen Electrode (RHE) in 1.0 M H_2SO_4 solution at 1 mV sec^{-1} scan rate.

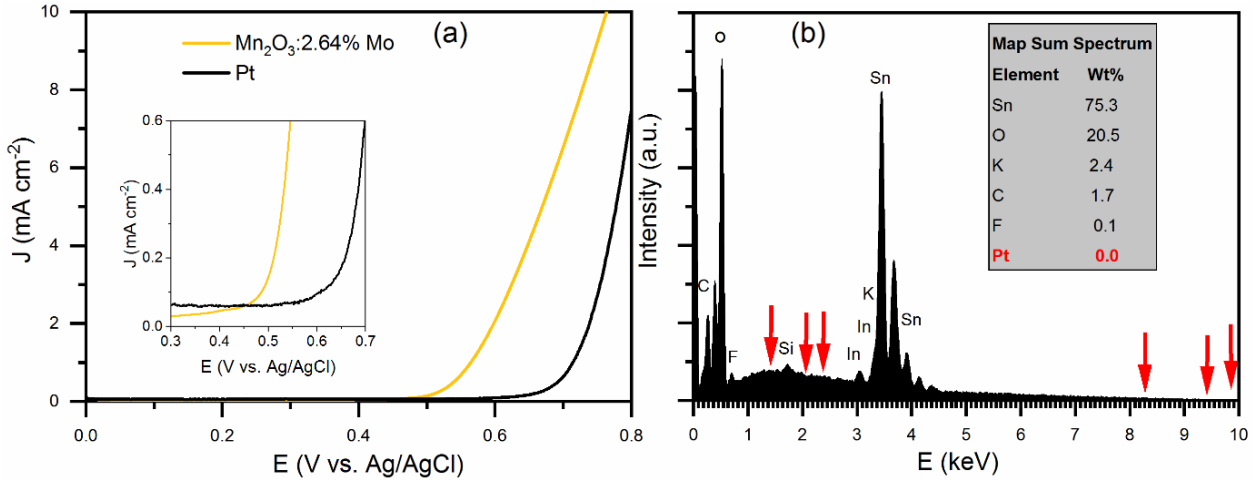

Figure S27. (a) LSV measurements of complete range and comparison of onset OER range (inset) of Pt and Mn_2O_3:2.64%Mo working electrodes in a three electrode setup using Pt-mesh as counter and Ag/AgCl as reference electrode in 1 M KOH. (b) Postcatalytic EDX analysis of blank FTO working electrode. The red arrows indicate the Pt edges in the EDX spectrum.

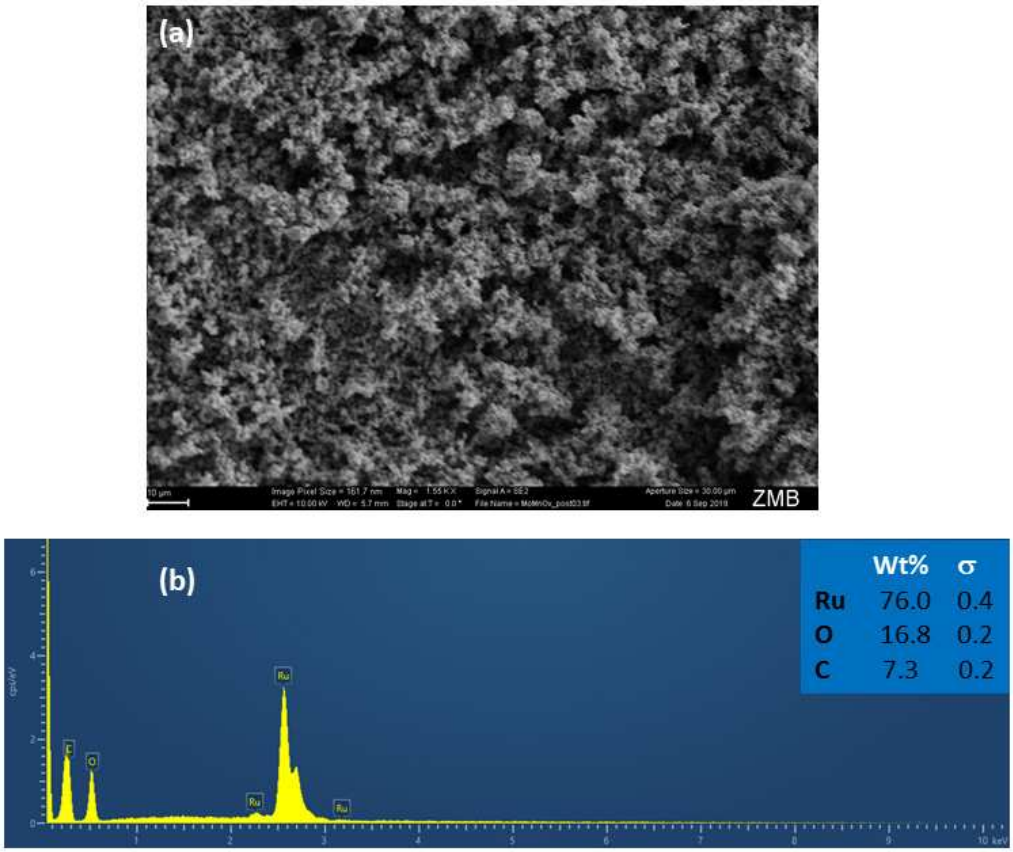

Figure S28. SEM image (a) and EDX spectrum (b) of RuO_2. Carbon content is from the SEM sample holder (Source: Ruthenium(IV) oxide, 99.9% trace metal basis (Sigma Aldrich product no.: 238058).

References

(1) Frey, C. E.; Kurz, P. Water Oxidation Catalysis by Synthetic Manganese Oxides with Different Structural Motifs: A Comparative Study. *Chem. Eur. J.* **2015**, *21*, 14958–14968.

(2) Robinson, D. M.; Go, Y. B.; Mui, M.; Gardner, G.; Zhang, Z.; Mastrogiovanni, D.; Garfunkel, E.; Li, J.; Greenblatt, M.; Dismukes, G. C. Photochemical water oxidation by crystalline polymorphs of manganese oxides: structural requirements for catalysis. *J. Am. Chem. Soc.* **2013**, *135*, 3494–3501.

(3) Pickrahn, K. L.; Park, S. W.; Gorlin, Y.; Lee, H.-B.-R.; Jaramillo, T. F.; Bent, S. F. Active MnO_x Electrocatalysts Prepared by Atomic Layer Deposition for Oxygen Evolution and Oxygen Reduction Reactions. *Adv. Energy Mater.* **2012**, *2*, 1269–1277.

(4) Yan, G.; Lian, Y.; Gu, Y.; Yang, C.; Sun, H.; Mu, Q.; Li, Q.; Zhu, W.; Zheng, X.; Chen, M.; Zhu, J.; Deng, Z.; Peng, Y. Phase and Morphology Transformation of MnO_2 Induced by Ionic Liquids toward Efficient Water Oxidation. *ACS Catal.* **2018**, *8*, 10137–10147.

(5) Antoni, H.; Morales, D. M.; Fu, Q.; Chen, Y.-T.; Masa, J.; Schuhmann, W.; Muhler, M. Oxidative Deposition of Manganese Oxide Nanosheets on Nitrogen-Functionalized Carbon Nanotubes Applied in the Alkaline Oxygen Evolution Reaction. *ACS Omega* **2018**, *3*, 11216–11226.

(6) Kang, Q.; Vernisse, L.; Remsing, R. C.; Thenuwara, A. C.; Shumlas, S. L.; McKendry, I. G.; Klein, M. L.; Borguet, E.; Zdilla, M. J.; Strongin, D. R. Effect of Interlayer Spacing on the Activity of Layered Manganese Oxide Bilayer Catalysts for the Oxygen Evolution Reaction. *J. Am. Chem. Soc.* **2017**, *139*, 1863–1870.

(7) Zhao, Y.; Chang, C.; Teng, F.; Zhao, Y.; Chen, G.; Shi, R.; Waterhouse, G. I. N.; Huang, W.; Zhang, T. Defect-Engineered Ultrathin δ-MnO_2 Nanosheet Arrays as Bifunctional Electrodes for Efficient Overall Water Splitting. *Adv. Energy Mater.* **2017**, *7*, 1700005-(1)-1700005-(7).

(8) Han, G.-Q.; Liu, Y.-R.; Hu, W.-H.; Dong, B.; Li, X.; Shang, X.; Chai, Y.-M.; Liu, Y.-Q.; Liu, C.-G. Crystallographic Structure and Morphology Transformation of MnO_2 Nanorods as Efficient Electrocatalysts for Oxygen Evolution Reaction. *J. Electrochem. Soc.* **2016**, *163*, H67-H73.

(9) Luo, X.-F.; Wang, J.; Liang, Z.-S.; Chen, S.-Z.; Liu, Z.-L.; Xu, C.-W. Manganese oxide with different morphology as efficient electrocatalyst for oxygen evolution reaction. *Int. J. Hydrogen Energy* **2017**, *42*, 7151–7157.

(10) Li, Y.-F.; Liu, Z.-P. Active Site Revealed for Water Oxidation on Electrochemically Induced δ-MnO_2: Role of Spinel-to-Layer Phase Transition. *J. Am. Chem. Soc.* **2018**, *140*, 1783–1792.

(11) Wang, L.; Qin, M.; Yang, W.; Gao, Y.; Li, Y. Efficient Electrochemical Water Oxidation and Oxidative Degradation of Rhodamine B: A Comparative Study Using High-Purity Birnessites Containing Li^+, Na^+ or K^+ Ions. *ChemistrySelect* **2017**, *2*, 5587–5594.

(12) Lübke, M.; Sumboja, A.; McCafferty, L.; Armer, C. F.; Handoko, A. D.; Du, Y.; McColl, K.; Cora, F.; Brett, D.; Liu, Z.; Darr, J. A. Transition-Metal-Doped α-MnO_2 Nanorods as Bifunctional Catalysts for Efficient Oxygen Reduction and Evolution Reactions. *ChemistrySelect* **2018**, *3*, 2613–2622.

(13) Simchi, H.; Cooley, K. A.; Ohms, J.; Huang, L.; Kurz, P.; Mohney, S. E. Cosputtered Calcium Manganese Oxide Electrodes for Water Oxidation. *Inorg. Chem.* **2018**, *57*, 785–792.

(14) Li, N.; Xia, W.-Y.; Wang, J.; Liu, Z.-L.; Li, Q.-Y.; Chen, S.-Z.; Xu, C.-W.; Lu, X.-H. Manganese oxides supported on hydrogenated TiO_2 nanowire array catalysts for the electrochemical oxygen evolution reaction in water electrolysis. *J. Mater. Chem. A* **2015**, *3*, 21308–21313.

(15) Meng, Y.; Song, W.; Huang, H.; Ren, Z.; Chen, S.-Y.; Suib, S. L. Structure-property relationship of bifunctional MnO_2 nanostructures: highly efficient, ultra-stable electrochemical water oxidation and oxygen reduction reaction catalysts identified in alkaline media. *J. Am. Chem. Soc.* **2014**, *136*, 11452–11464.

(16) Fekete, M.; Hocking, R. K.; Chang, S. L. Y.; Italiano, C.; Patti, A. F.; Arena, F.; Spiccia, L. Highly active screen-printed electrocatalysts for water oxidation based on β-manganese oxide. *Energy Environ. Sci.* **2013**, *6*, 2222–2232.

(17) Ramírez, A.; Hillebrand, P.; Stellmach, D.; May, M. M.; Bogdanoff, P.; Fiechter, S. Evaluation of MnO_x, Mn_2O_3, and Mn_3O_4 Electrodeposited Films for the Oxygen Evolution Reaction of Water. *J. Phys. Chem. C* **2014**, *118*, 14073–14081.

(18) Jin, K.; Chu, A.; Park, J.; Jeong, D.; Jerng, S. E.; Sim, U.; Jeong, H.-Y.; Lee, C. W.; Park, Y.-S.; Yang, K. D.; Kumar Pradhan, G.; Kim, D.; Sung, N.-E.; Hee Kim, S.; Nam, K. T. Partially Oxidized Sub-10 nm MnO Nanocrystals with High Activity for Water Oxidation Catalysis. *Sci. Rep.* **2015**, *5*, 10279-(1)-10279-(11).

(19) Wang, Q.; Hu, W.; Huang, Y. Nitrogen doped graphene anchored cobalt oxides efficiently bi-functionally catalyze both oxygen reduction reaction and oxygen revolution reaction. *Int. J. Hydrogen Energy* **2017**, *42*, 5899–5907.

(20) Ji, X.; Hao, S.; Qu, F.; Liu, J.; Du, G.; Asiri, A. M.; Chen, L.; Sun, X. Core-shell $CoFe_2O_4$@Co-Fe-Bi nanoarray: a surface-amorphization water oxidation catalyst operating at near-neutral pH. *Nanoscale* **2017**, *9*, 7714–7718.

(21) Xiao, C.; Li, Y.; Lu, X.; Zhao, C. Bifunctional Porous NiFe/$NiCo_2O_4$/Ni Foam Electrodes with Triple Hierarchy and Double Synergies for Efficient Whole Cell Water Splitting. *Adv. Funct. Mater.* **2016**, *26*, 3515–3523.

(22) Liang, H.; Gandi, A. N.; Xia, C.; Hedhili, M. N.; Anjum, D. H.; Schwingenschlögl, U.; Alshareef, H. N. Amorphous NiFe-OH/NiFeP Electrocatalyst Fabricated at Low Temperature for Water Oxidation Applications. *ACS Energy Lett.* **2017**, *2*, 1035–1042.

(23) Konkena, B.; Masa, J.; Botz, A. J. R.; Sinev, I.; Xia, W.; Koßmann, J.; Drautz, R.; Muhler, M.; Schuhmann, W. Metallic $NiPS_3$@NiOOH Core–Shell Heterostructures as Highly Efficient and Stable Electrocatalyst for the Oxygen Evolution Reaction. *ACS Catal.* **2017**, *7*, 229–237.

(24) Fan, K.; Chen, H.; Ji, Y.; Huang, H.; Claesson, P. M.; Daniel, Q.; Philippe, B.; Rensmo, H.; Li, F.; Luo, Y.; Sun, L. Nickel-vanadium monolayer double hydroxide for efficient electrochemical water oxidation. *Nat. Commun.* **2016**, *7*, 11981-(1)-11981-(9).

(25) Zou, X.; Liu, Y.; Li, G.-D.; Wu, Y.; Liu, D.-P.; Li, W.; Li, H.-W.; Wang, D.; Zhang, Y.; Zou, X. Ultrafast Formation of Amorphous Bimetallic Hydroxide Films on 3D Conductive Sulfide Nanoarrays for Large-Current-Density Oxygen Evolution Electrocatalysis. *Adv. Mater.* **2017**, *29*, 1700404-(1)-1700404-(7).
(26) Gore, C. M.; White, J. O.; Wachsman, E. D.; Thangadurai, V. Effect of composition and microstructure on electrical properties and CO_2 stability of donor-doped, proton conducting $BaCe_{1-(x+y)}Zr_xNb_yO_3$. *J. Mater. Chem. A* **2014**, *2*, 2363–2373.
(27) Irvine, J. T. S.; Sinclair, D. C.; West, A. R. Electroceramics: Characterization by Impedance Spectroscopy. *Adv. Mater.* **1990**, *2*, 132–138.
(28) Li, Q.; Thangadurai, V. Synthesis, Structure and Electrical Properties of Mo-doped CeO_2Materials for SOFCs. *Fuel Cells* **2009**, *9*, 684–698.
(29) Xie, F.; Meng, H.; Shen, P. K. Diffusion study in a novel three-dimensional electrode for direct methanol fuel cells. *Electrochim. Acta* **2008**, *53*, 5039–5044.
(30) Mukherjee, D.; Austeria, P. M.; Sampath, S. Two-Dimensional, Few-Layer Phosphochalcogenide, $FePS_3$: A New Catalyst for Electrochemical Hydrogen Evolution over Wide pH Range. *ACS Energy Lett.* **2016**, *1*, 367–372.
(31) Deng, J.; Ren, P.; Deng, D.; Yu, L.; Yang, F.; Bao, X. Highly active and durable non-precious-metal catalysts encapsulated in carbon nanotubes for hydrogen evolution reaction. *Energy Environ. Sci.* **2014**, *7*, 1919–1923.